

Helical flow states in active nematics

Ryan R. Keogh,¹ Santhan Chandragiri², Benjamin Loewe¹, Tapio Ala-Nissila^{3,4},
Sumesh P. Thampi² and Tyler N. Shendruk^{1,*}

¹*School of Physics and Astronomy, The University of Edinburgh, Peter Guthrie Tait Road, Edinburgh EH9 3FD, United Kingdom*

²*Department of Chemical Engineering, Indian Institute of Technology Madras, Chennai 600036, India*

³*MSP Group, QTF Centre of Excellence, Department of Applied Physics, Aalto University, P.O. Box 11000, FI-00076 Aalto, Espoo, Finland*

⁴*Interdisciplinary Centre for Mathematical Modelling, Department of Mathematical Sciences, Loughborough University, Loughborough LE11 3TU, United Kingdom*

 (Received 2 December 2021; revised 17 February 2022; accepted 9 June 2022; published 7 July 2022)

We show that confining extensile nematics in three-dimensional (3D) channels leads to the emergence of two self-organized flow states with nonzero helicity. The first is a pair of braided antiparallel streams—this *double helix* occurs when the activity is moderate, anchoring negligible, and reduced temperature high. The second consists of axially aligned counter-rotating vortices—this *grinder train* arises between spontaneous axial streaming and the vortex lattice. These two unanticipated helical flow states illustrate the potential of active fluids to break symmetries and form complex but organized spatiotemporal structures in 3D fluidic devices.

DOI: [10.1103/PhysRevE.106.L012602](https://doi.org/10.1103/PhysRevE.106.L012602)

Because active materials are composed of microscopic constituents, which locally transmute internal energy into mechanical forces that are dissipated by the surrounding medium, they can possess broken symmetries and emergent dynamic properties on macroscopic scales. These self-organized, *active dissipative structures* have been observed to take many forms. The premier example of activity-induced dissipative structures is the flocking of polar particles [1–3], in which a liquid-gas-like transition [4] from disorderly to collective motion is associated with spontaneous spatial phase separation [5]. In addition to coexistence, hexatic, smectic, and solid phases can originate from activity [6,7]. Likewise, activity can generate orientational order [8,9], including active alignment of motile rods [10,11] and swimming bacilliforms [12].

Activity can also induce self-organized flow states [13]. In confining channels, an extensile active stress-induced instability to bend perturbations leads to self-sustained spontaneous flows [14–18] and spontaneous circulations [19–21] when the characteristic activity length scale ℓ_{act} is comparable to the confinement size L , as seen in numerous experimental systems [22–29]. Vortex lattices arise when the characteristic length scale matches the confinement, which can be due to an array of obstacles or cavities [30–35], bound to spherical surfaces [36], or channel confinement [37–40]. Local circulations arise because ℓ_{act} represents the characteristic vorticity length scale [41], associated with a peak in the enstrophy distribution [42–45], and a lattice of vortices represents stress-free solutions that lie at the interface of the stable and unstable modes in minimal continuum models of active fluids [46]. Such two-dimensional (2D) flow states represent the emergence of a broken translational symmetry of the vorticity field.

However, three-dimensional (3D) fluids possess the capacity for flows that are not allowed in 2D. *Helicity*, for instance, is identically zero in 2D and has not previously been observed to spontaneously break symmetry in response to activity. One reason for this apparent absence is simply because much of the theoretical, computational, and experimental work on active nematics is on 2D films. However, the recent advent of experimentally realizable 3D active nematics [47] has spurred immediate interest in active liquid crystals beyond films [48–55]. By removing the dimensional limitations of confinement in 2D, additional classes of self-organized flows states may be possible. We report long-lived, nonzero helical active dissipative 3D structures that spontaneously break chiral symmetry.

We numerically confine active nematics in square ducts of size L defined by four impermeable, no-slip walls. The square-duct geometry is utilized to produce quasi-1D confinement without curved boundaries [56–58]. We vary the extensile activity, reduced temperature, and anchoring strength on the channel walls. When the anchoring is weak and reduced temperature is high, we find a *double-helix* flow structure, in which two streams of antiparallel flow braid around one another, spontaneously breaking chiral symmetry [Fig. 1(a); Movie 1 [59]]. When the anchoring strength is strong, we find a *grinder train* flow structure, in which a lattice of axially aligned, counter-rotating vortices drift down the channel with nonzero helicity [Fig. 1(b); Movie 2 [59]]. Both flow states are helical, span the entire system, and are long lived. The self-organization of helicity from a system with nematic symmetry highlights the potential of activity as a pathway for designing emergent, material dynamics. Spontaneous chiral symmetry breaking is characteristic of helix formation, which extends beyond active fluids.

In our model of an active nematic fluid, the nondimensionalized velocity $\vec{u}(\vec{r}; t)$ and nematic order $\mathbf{Q}(\vec{r}; t)$ are coupled,

*t.shendruk@ed.ac.uk

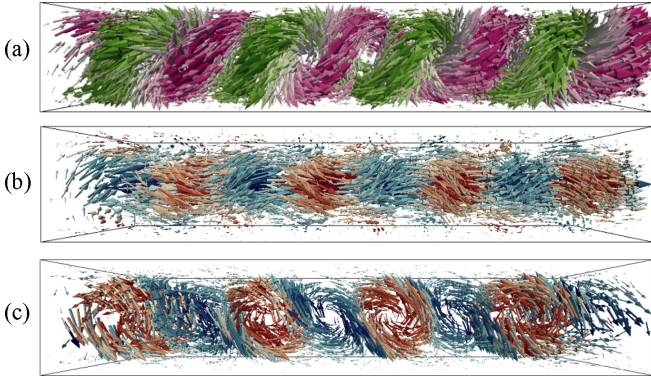


FIG. 1. Active dissipative flow structures exhibiting rotational flow. (a) Double helix: Two streams of antiparallel flow braid around one another for parameters $\tilde{P} = \{\tilde{K}^{-1/2}, \tilde{W}, \tilde{T}^{1/2}\} = \{25, 1.5, 9.47\}$. Colored by axial velocity u_{\parallel} [see Movie 1 in the Supplemental Material (SM) [59]]. (b) Grinder train: Procession of spontaneously drifting, counter-rotating vortices aligned axially down the duct for $\tilde{P} = \{20, 250, 0\}$. Colored by axial vorticity ω_{\parallel} (Movie 2 [59]). (c) Ceilidh vortex: Vortex lattice oriented in the transverse direction for $\tilde{P} = \{22, 250, 0\}$. Colored by transverse vorticity ω_{\perp} (Movie 3 [59]).

and density is constant [60–62]. The dimensionless Cauchy equation balances the material derivative of velocity against the divergence of the stress, $\tilde{\rho} D_t \tilde{u} = \tilde{\nabla} \cdot \tilde{\Pi}$. Since the active contribution to the stress $-\zeta \mathbf{Q}$ drives spontaneous nematic distortions on length scales ℓ_{act} and flows of speed U , we nondimensionalize each term by the activity ζ , resulting in the active inertia number $\tilde{\rho} = \rho U^2 / \zeta$ for density ρ . Two additional dimensionless numbers appear from the stress divergence—dimensionless viscosity [Eq. SM(3) [59]] and, more relevantly, the *activity number* $\tilde{K}^{-1/2} = L / \ell_{\text{act}}$, where $\ell_{\text{act}} \sim \sqrt{K / \zeta}$ is the characteristic activity length due to the competition of activity ζ and nematic elasticity K .

The evolution equation for the nematic orientation $D_t \mathbf{Q} - \mathcal{S} = \tilde{\Gamma} \mathcal{H}$, in which the covariant derivative (including a corotational advection term \mathcal{S}) is balanced by the relaxation towards equilibrium, characterized by an inverse nematic Péclet number $\tilde{\Gamma}$. The molecular field \mathcal{H} has contributions due to the bulk (characterized by the lowest-order Landau free-energy coefficient A), distortions (by K), and surface anchoring (by anchoring strength W). Nondimensionalizing these by the distortion free-energy scale produces two dimensionless numbers—the distance from the passive-thermodynamic isotropic-nematic transition, which is a reduced temperature $\tilde{T}^{1/2} = L / \sqrt{K/A}$, and the strength of the degenerate planar anchoring, which can be measured as $\tilde{W} = L / (K/W)$, as in colloidal liquid crystals [63]. Further technical details of the model are provided in SM 1 [59].

Non-dimensionalized parameter space is denoted by

$$\tilde{P} = \{\tilde{K}^{-1/2}, \tilde{W}, \tilde{T}^{1/2}\} \equiv \left\{ \sqrt{\frac{\zeta}{K}} L, \frac{W}{K} L, \sqrt{\frac{A}{K}} L \right\}, \quad (1)$$

each component of which can be interpreted as a ratio of system size to a characteristic length scale (SM 2 [59]). By varying the anchoring strength \tilde{W} and reduced temperature

$\tilde{T}^{1/2}$, the simulations explore regions of parameter space that have previously not received adequate attention.

For sufficiently small extensile activity ($\tilde{K}^{-1/2} \lesssim 18$), we find spontaneous streaming in the axial direction. These are unidirectional and oscillating flows, which have been well documented in 2D channels [17,37,64]. Here, we do not delineate between these but refer to both as *axial streaming*. At sufficiently large activity, mesoscale or *active turbulence* occurs. In active turbulence, the components of vorticity $\tilde{\omega} = \tilde{\nabla} \times \tilde{u}$ in the axial and two transverse directions (denoted by subscript \parallel and $\perp_{1,2}$, respectively) are isotropic—the probability distributions of the axial ω_{\parallel} and transverse $\omega_{\perp_{1,2}}$ components of the vorticity are equivalent [Fig. 2(d)]. The distributions are symmetric about zero and normal.

The active dissipative structures exist in the intermediate regime between axial streaming and active turbulence, where the active length scale ℓ_{act} is comparable to the confinement length L . The most common of these dissipative structures is a nonhelical lattice of counter-rotating vortices oriented transverse to the channel, breaking translational symmetry [Fig. 1(c)]. This is the 3D equivalent of the 2D Ceilidh dynamic state [37,38]. The 3D Ceilidh lattice exhibits dancing disclinations; however, these are now curved disclination lines that span the channel (Movie 4 [59]). As a vortex lattice, the vorticity distribution is strongly bimodal [Fig. 2(c)]. The ω_{\perp_2} distribution is symmetric about zero and bimodal with prominent peaks, representing the lattice of counter-rotating vortices with spontaneous symmetry breaking between the two transverse directions. There is negligible vorticity in both the other directions.

While the grinder train is similar to the Ceilidh lattice, the crucial distinction is that the counter-rotating vortices are oriented axially, rather than transversely [Fig. 1(b); Movie 2 [59]]. Similar to axial streaming states [13,51], the grinder train has a net flow along the channel. This flow structure is a train of axially aligned counter-rotating vortices drifting down the axis of the channel that exists when anchoring is strong (Movie 2 [59]). Thus, the distributions of vorticity are similar to the Ceilidh vortex, except the bimodal distribution is narrower and in the axial direction ω_{\parallel} , rather than a transverse direction [Fig. 2(b)]. Though both the Ceilidh lattice and the grinder train manifest counter-rotating vortices and both break translational symmetry, the Ceilidh lattice does not possess local helicity $H = \tilde{u} \cdot \tilde{\omega}$ in contrast to the grinder train [Fig. 3(a)]. The instantaneous centerline helicity forms a well-defined wave [Fig. 3(c)] and the drift exhibits temporal oscillation [Fig. 3(d); Movie 5 [59]], reflecting the steady motion of the helicity train. The steady translation, but oscillating sign, of the helicity indicates the grinder is a lattice of counter-rotating vortices.

Qualitatively, the grinder train possesses characteristics of both axial streaming and vorticity translational symmetry breaking. Indeed, as the axial streaming begins to oscillate on scales comparable to the confinement, counter-rotating vortices can align axially, resulting in nonzero local helicity—though the average is zero (Movie 6 [59]), the distribution is bimodal [Fig. 3(b)]. It also generates smaller vorticity [Figs. 2(b) and 2(c)] due to the fact that it possesses less nematic distortions and is entirely free of disclinations (Movie 4 [59]).

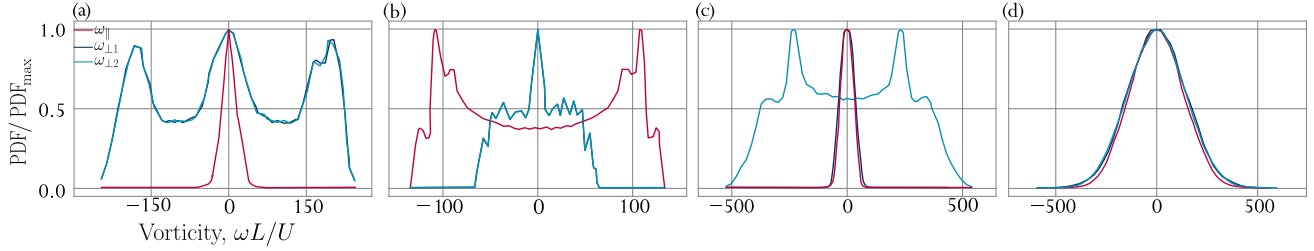


FIG. 2. Probability distributions of vorticity for active dissipative flow structures at parameters $\vec{P} = \{\tilde{K}^{-1/2}, \tilde{W}, \tilde{T}^{1/2}\}$. The components are the vorticity taken about the centerline in the axial direction ω_{\parallel} (red lines) and in the two transverse directions $\omega_{\perp,1,2}$ (blue and cyan lines) averaged over ten random initializations. (a) The double helix ($\vec{P} = \{25, 1.5, 9.47\}$) possesses nonzero vorticity in both transverse directions $\omega_{\perp,1,2}$. (b) Grinder train ($\vec{P} = \{20, 250, 0\}$). (c) The Ceilidh vortex lattice ($\vec{P} = \{22, 250, 0\}$) possesses nonzero vorticity only in one of the two transverse directions. (d) Turbulent flow ($\vec{P} = \{25, 250, 0\}$) is nearly isotropic.

On the other hand, the double helix does possess large nematic distortions: A clear cork-screw disclination line spirals through the center of the channel (Movie 4 [59]). This is because the grinder train exists at strong anchoring, while the double helix exists at weak anchoring and high reduced temperature, which leads to more disorderly helicity fields [Fig. 3(d); Movie 6 [59]]. The helicity is largest far from the no-slip boundaries. We find double helices most frequently in regions of high reduced temperature $\tilde{T}^{1/2}$, suggesting that the double helix emerges when the thermodynamic persistence length is comparable to the confinement size. Unlike the Ceilidh or grinder lattices, the double helix is not composed of isolated vortices and so the centerline helicity does not exhibit a clear spatiotemporal structure [Figs. 3(c) and 3(d)].

Additionally, the vorticity of the double-helix state is smallest in the axial direction and not strongly bimodal in the two transverse directions [Fig. 2(a)]. Unlike the grinder train, the helicity distribution is primarily unimodal [Fig. 3(b)]. Since it is composed of a pair of helices with opposite handedness but also opposite streaming directions, the double helix spontaneously breaks chiral symmetry.

To map the existence of helical flow in parameter space, we characterize the flow states by their associated length scales and helicity. The nonhelical Ceilidh vortex lattice is long lived and system spanning, with spatial persistence clear from the velocity-velocity autocorrelation function C_{uu} (SM 3 [59]) down the length of the channel [Fig. 4(a); blue squares], exhibiting long-range oscillating correlations. Dissimilarly, the correlation function of the turbulent state rapidly decorrelates [Fig. 4(a); blue circles]. While the correlation functions of these two intercept zero (Fig. 4; solid symbols), the axial streaming state initially decays to a long-range constant value [Fig. 4(a); open pink circles] and the grinder train possesses long-range oscillating correlations about a nonzero value [Fig. 4(a); open purple squares]. The correlation function of the grinder train has a longer period but smaller amplitude than the Ceilidh lattice and does not decorrelate [Fig. 4(a)] since the grinder train state appears between axial streaming and the vortex lattice [Fig. 4(b)].

The active dissipative structures are identified by the length scales characterizing the flows ℓ_u , measured from the velocity correlations (SM 3 [59]). The length scales reveal distinct transitions between each flow state [Fig. 4(b)]. The Ceilidh lattice occupies the largest region of the activity-anchoring phase plane [Fig. 4(c)]. The phase diagram demonstrates that axial streaming exists for all anchoring numbers at sufficiently small activity. The activity at which the flow transitions from axial streaming is only weakly dependent on anchoring strength across many orders of magnitude [Fig. 4(c)]. For moderate to weak anchoring, the Ceilidh lattice is the only dissipative structure between axial streaming and active turbulence.

The grinder train arises because the anchoring suppresses the formation of the dancing disclination lines that are present in the vortex lattice. This reduction in nematic distortion lowers the vorticity magnitude and makes the flow deterministic, such that the transverse directions coincide [Fig. 2(b)]. However, it does not alter the match between the characteristic

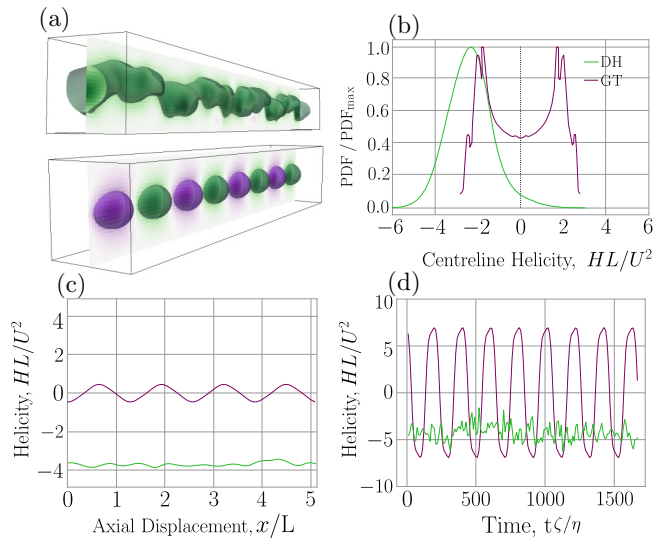


FIG. 3. Local helicity $H = \vec{u} \cdot \vec{\omega}$ for the double helix ($\vec{P} = \{25, 0.0015, 6.5\}$) and grinder train ($\vec{P} = \{25, 250, 0\}$) flow states. (a) Snapshots showing the helicity field as a 3D isosurface through the center plane of the duct. Top: Double helix with negative chirality (Movie 6 [59]). Bottom: Grinder train with alternating chirality (Movie 5 [59]). (b) Distributions of helicity down the channel centerline averaged over ten random initializations. (c) Spatial variation of instantaneous cross-sectional averaged helicity. (d) Temporal variation of cross-sectional averaged helicity at a single point. (b)–(d) Double helix is shown in green and the grinder train in purple.

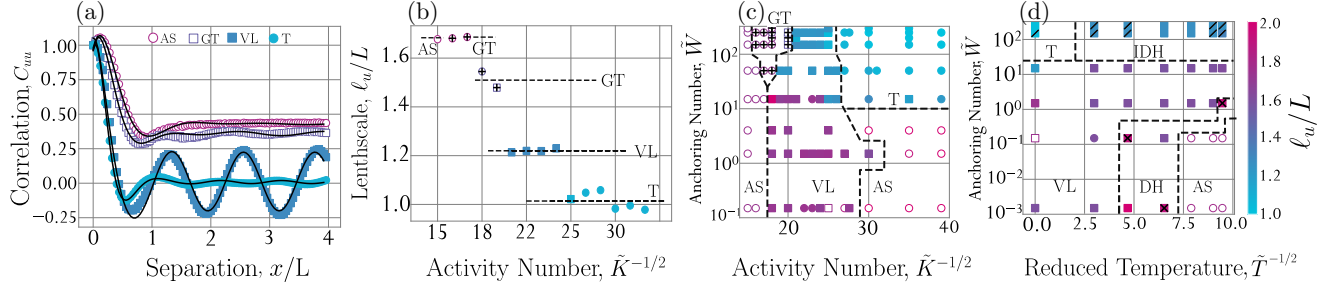


FIG. 4. Active dissipative structure phase diagrams. (a) Spatial velocity-velocity correlations along the channel centerline for $\tilde{P} = \{\tilde{K}^{-1/2}, 250, 0\}$ for various $\tilde{K}^{-1/2}$. Example curves for axial streaming (AS; $\tilde{K}^{-1/2} = 15$), grinder train (GT; $\tilde{K}^{-1/2} = 20$), vortex lattice (VL; $\tilde{K}^{-1/2} = 15$), and mesoscale turbulence (T; $\tilde{K}^{-1/2} = 15$). Open symbols denote nonzero long-range correlations, while square symbols denote long-range oscillations with nonzero amplitude. (b) Characteristic length scale ℓ_u determined from the autocorrelation functions (SM 3 [59]) for $\tilde{P} = \{\tilde{K}^{-1/2}, 250, 0\}$. \boxplus marks large values of peak resolution [Eq. SM (25) [59]]. (c) The length scales ℓ_u as a function of dimensionless extensile activity $\tilde{K}^{-1/2}$ and planar anchoring \tilde{W} for reduced temperature $\tilde{T}^{1/2} = 0$. (d) Length scales as a function of \tilde{W} and $\tilde{T}^{1/2}$ for $\tilde{K}^{-1/2} = 25$. Markers denote for average system helicity (SM 5 [59]): \boxtimes denotes large average helicity $H_{(0)}$ and \boxminus indicates large values of the average of the magnitude of $H_{(0)}$, which respectively identify regions for the double helix (DH) and intermittent double helix (IDH).

vortex size ℓ_{act} and the confinement L . Thus, the vortices preferentially lie axially along the channel.

When the reduced temperature $\tilde{T}^{1/2}$ is increased above the isotropic-nematic transition, the fluid can still be dynamically oriented by the active flows [8,9]. Indeed, vortex lattices exist for a wide range of $\tilde{T}^{1/2}$ and \tilde{W} at $\tilde{K}^{-1/2} = 25$ [Fig. 4(d)]. However, in the low anchoring limit and at moderate reduced temperatures, the double-helix structure exists as a second region for which there is nonzero helicity. While the grinder train and double helix both exist for intermediate activity, the grinder train requires strong anchoring at $\tilde{T}^{1/2} = 0$ [Fig. 4(c)] and the double helix occurs for weak anchoring at high reduced temperatures [Fig. 4(d)].

In addition to the orderly double helix and grinder train, we identify a less structured, noisy regime at high reduced temperatures and strong anchoring [Fig. 4(d); slashes]. In this regime, we find intermittent double helices interspersed with more chaotic behavior (Movie 7 [59]). Naturally, the stochasticity in these systems results in inconsistent helicity but higher fluid speeds, resulting in lower average helicity.

To understand the origin of active helical structures, we derive the dimensionless transport equation for helicity,

$$\tilde{\rho} D_t H + \tilde{\nabla} \cdot \tilde{J} = \Sigma, \quad (2)$$

with helicity flux \tilde{J} and source terms Σ (see SM 4 [59]). By calculating the dimensionless numbers associated with each source [Eqs. SM(18)–SM(21) [59]], we find that the nematic and viscous sources are negligible compared to the activity-induced helicity source $\Sigma^a = -\tilde{\omega} \cdot [\tilde{\nabla} \cdot \mathbf{Q}] - \tilde{u} \cdot (\tilde{\nabla} \times [\tilde{\nabla} \cdot \mathbf{Q}])$. The first active source term emerges from the projection of active force onto the vorticity field, while the second term represents projection of the curl of the active force onto the velocity field. In both helical flow states, the two active terms are of the same magnitude (Fig. SM6 [59]). Immediately following initialization, the transient grinder train structure begins as oscillating discoidal regions of Σ^a (Movie 8 [59]). Once the drifting grinder train forms, Σ^a takes the form of a traveling wave that produces the drifting train of

alternating helicity (Fig. 3). Similarly for the double helix, the active source forms local regions of production and elimination (Movie 9 [59]), which are associated with the cork-screw disclination. Indeed, in stark contrast to the defect dancing observed in the Ceilidh vortex lattice state, the grinder train does not possess any topological singularities, while the double helix possesses a single disclination line that winds through the two helical flows.

Recent work on 3D active nematics [48–55] has shown them to be complicated by their tangle of 3D disclination lines. However, they also possess the potential for an exciting range of possible dissipative structures. We have shown a simple case with the emergence of two spontaneous, long-lived, nonzero helicity structures in simple confinement for extensile activity, planar anchoring and non-negative reduced temperature. In driven systems, double helical flow states can exhibit complex nonlinear dynamics [65] and control the dispersivity of particles eluting in streams [66]. In fact, surface-activity driven helical flows have been identified and analyzed in the context of cytoplasmic streaming [67–70]. In these cases of long plant cells, helical flow enables significant transport, mixing, and enhanced rates of nutrient exchange with the surrounding membrane [67]. Indeed, recent work has considered defect dynamics [71] and helical flows [72] on cylindrical surfaces. Spontaneous chiral symmetry breaking is a characteristic aspect of helix formation in such material dynamics, which extends beyond the sphere of active fluids. For example, chirality has been shown to be relevant in morphological processes, such as the gastrulation of *Drosophila* embryos, in which gut formation acquires spontaneous left-right asymmetry that leads to twisting [73]. Likewise, the mitotic spindle, which has been modeled as an active nematic [74], exhibits chirality [75]. Furthermore, spontaneous chiral symmetry breaking has been observed in the director field of passive achiral nematics subject to strong confinements [76–79].

The experimental realization of 3D active nematics [47] promises many opportunities to explore active dissipative structures that were not possible in 2D and helicity may play a key role in many such structures, as suggested by these results.

Helicity is involved in energy cascades in active turbulence [80] and generally plays an important role in characterizing the topological nature of 3D flows [81]. This Letter reports spontaneous chiral symmetry breaking in active nematics leading to a steady state helical flow.

We thank Kevin Stratford and Kristian Thijssen for invaluable help. This research has received funding (TNS) from the

European Research Council under the European Union's Horizon 2020 research and innovation programme (Grant Agreement No. 851196). S.P.T. acknowledges the support by the Department of Science and Technology, India, via Research Grant No. CRG/2018/000644. T.A.-N. has been supported in part by the Academy of Finland PolyDyna (No. 307806) and QFT Center of Excellence Program grant (No. 312298).

-
- [1] T. Vicsek, A. Czirók, E. Ben-Jacob, I. Cohen, and O. Shochet, *Phys. Rev. Lett.* **75**, 1226 (1995).
- [2] J. Toner and Y. Tu, *Phys. Rev. Lett.* **75**, 4326 (1995).
- [3] J. Toner and Y. Tu, *Phys. Rev. E* **58**, 4828 (1998).
- [4] A. P. Solon, H. Chaté, and J. Tailleur, *Phys. Rev. Lett.* **114**, 068101 (2015).
- [5] H. Chaté, F. Ginelli, G. Grégoire, and F. Raynaud, *Phys. Rev. E* **77**, 046113 (2008).
- [6] P. Digregorio, D. Levis, A. Suma, L. F. Cugliandolo, G. Gonnella, and I. Pagonabarraga, *Phys. Rev. Lett.* **121**, 098003 (2018).
- [7] J. Chattopadhyay, S. Pannir-Sivajothi, K. Varma, S. Ramaswamy, C. Dasgupta, and P. K. Maiti, *Phys. Rev. E* **104**, 054610 (2021).
- [8] S. Santhosh, M. R. Nejad, A. Doostmohammadi, J. M. Yeomans, and S. P. Thampi, *J. Stat. Phys.* **180**, 699 (2020).
- [9] M. G. Giordano, F. Bonelli, L. N. Carenza, G. Gonnella, and G. Negro, *Europhys. Lett.* **133**, 58004 (2021).
- [10] M. Bär, R. Großmann, S. Heidenreich, and F. Peruani, *Annu. Rev. Condens. Matter Phys.* **11**, 441 (2020).
- [11] A. M. Nagel, M. Greenberg, T. N. Shendruk, and H. W. de Haan, *Sci. Rep.* **10**, 10747 (2020).
- [12] D. Nishiguchi, K. H. Nagai, H. Chaté, and M. Sano, *Phys. Rev. E* **95**, 020601(R) (2017).
- [13] R. Voituriez, J. F. Joanny, and J. Prost, *Phys. Rev. Lett.* **96**, 028102 (2006).
- [14] R. Voituriez, J. F. Joanny, and J. Prost, *Europhys. Lett.* **70**, 404 (2005).
- [15] S. Ramaswamy and M. Rao, *New J. Phys.* **9**, 423 (2007).
- [16] S. A. Edwards and J. M. Yeomans, *Europhys. Lett.* **85**, 18008 (2009).
- [17] S. M. Fielding, D. Marenduzzo, and M. E. Cates, *Phys. Rev. E* **83**, 041910 (2011).
- [18] M. Ravnik and J. M. Yeomans, *Phys. Rev. Lett.* **110**, 026001 (2013).
- [19] F. G. Woodhouse and R. E. Goldstein, *Phys. Rev. Lett.* **109**, 168105 (2012).
- [20] H. Jiang, H. Ding, M. Pu, and Z. Hou, *Soft Matter* **13**, 836 (2017).
- [21] M. Theillard, R. Alonso-Matilla, and D. Saintillan, *Soft Matter* **13**, 363 (2017).
- [22] H. Wioland, F. G. Woodhouse, J. Dunkel, J. O. Kessler, and R. E. Goldstein, *Phys. Rev. Lett.* **110**, 268102 (2013).
- [23] E. Lushi, H. Wioland, and R. E. Goldstein, *Proc. Natl. Acad. Sci. USA* **111**, 9733 (2014).
- [24] K. Beppu, Z. Izri, J. Gohya, K. Eto, M. Ichikawa, and Y. T. Maeda, *Soft Matter* **13**, 5038 (2017).
- [25] M. M. Norton, A. Baskaran, A. Opatthalage, B. Langeslay, S. Fraden, A. Baskaran, and M. F. Hagan, *Phys. Rev. E* **97**, 012702 (2018).
- [26] A. E. Hamby, D. K. Vig, S. Safonova, and C. W. Wolgemuth, *Sci. Adv.* **4**, eaau0125 (2018).
- [27] A. Opatthalage, M. M. Norton, M. P. N. Juniper, B. Langeslay, S. A. Aghvami, S. Fraden, and Z. Dogic, *Proc. Natl. Acad. Sci. USA* **116**, 4788 (2019).
- [28] J. Hardouin, J. Laurent, T. Lopez-Leon, J. Ignés-Mullol, and F. Sagués, *Soft Matter* **16**, 9230 (2020).
- [29] K. Thijssen, D. A. Khaladj, S. A. Aghvami, M. A. Gharbi, S. Fraden, J. M. Yeomans, L. S. Hirst, and T. N. Shendruk, *Proc. Natl. Acad. Sci. USA* **118**, e2106038118 (2021).
- [30] S. P. Thampi, A. Doostmohammadi, T. N. Shendruk, R. Golestanian, and J. M. Yeomans, *Sci. Adv.* **2**, e1501854 (2016).
- [31] H. Wioland, F. G. Woodhouse, J. Dunkel, and R. E. Goldstein, *Nat. Phys.* **12**, 341 (2016).
- [32] H. Wioland, E. Lushi, and R. E. Goldstein, *New J. Phys.* **18**, 075002 (2016).
- [33] D. Nishiguchi, I. S. Aranson, A. Snezhko, and A. Sokolov, *Nat. Commun.* **9**, 4486 (2018).
- [34] H. Reinken, D. Nishiguchi, S. Heidenreich, A. Sokolov, M. Bär, S. H. Klapp, and I. S. Aranson, *Commun. Phys.* **3**, 76 (2020).
- [35] M. James, D. A. Suchla, J. Dunkel, and M. Wilczek, *Nat. Commun.* **12**, 5630 (2021).
- [36] D. Khoromskaia and G. P. Alexander, *New J. Phys.* **19**, 103043 (2017).
- [37] T. N. Shendruk, A. Doostmohammadi, K. Thijssen, and J. M. Yeomans, *Soft Matter* **13**, 3853 (2017).
- [38] A. Doostmohammadi, T. N. Shendruk, K. Thijssen, and J. M. Yeomans, *Nat. Commun.* **8**, 15326 (2017).
- [39] B. Zhang, B. Hilton, C. Short, A. Souslov, and A. Snezhko, *Phys. Rev. Research* **2**, 043225 (2020).
- [40] A. Samui, J. M. Yeomans, and S. P. Thampi, *Soft Matter* **17**, 10640 (2021).
- [41] E. J. Hemingway, P. Mishra, M. C. Marchetti, and S. M. Fielding, *Soft Matter* **12**, 7943 (2016).
- [42] H. H. Wensink, J. Dunkel, S. Heidenreich, K. Drescher, R. E. Goldstein, H. Löwen, and J. M. Yeomans, *Proc. Natl. Acad. Sci. USA* **109**, 14308 (2012).
- [43] V. Bratanov, F. Jenko, and E. Frey, *Proc. Natl. Acad. Sci. USA* **112**, 15048 (2015).
- [44] L. N. Carenza, L. Biferale, and G. Gonnella, *Europhys. Lett.* **132**, 44003 (2020).
- [45] R. Alert, J.-F. Joanny, and J. Casademunt, *Nat. Phys.* **16**, 682 (2020).
- [46] J. Słomka and J. Dunkel, *Phys. Rev. Fluids* **2**, 043102 (2017).
- [47] G. Duclos, R. Adkins, D. Banerjee, M. S. Peterson, M. Varghese, I. Kolvin, A. Baskaran, R. A. Pelcovits, T. R. Powers,

- A. Baskaran, F. Toschi, M. F. Hagan, S. J. Streichan, V. Vitelli, D. A. Beller, and Z. Dogic, *Science* **367**, 1120 (2020).
- [48] T. N. Shendruk, K. Thijssen, J. M. Yeomans, and A. Doostmohammadi, *Phys. Rev. E* **98**, 010601(R) (2018).
- [49] S. Čopar, J. Aplinc, Ž. Kos, S. Žumer, and M. Ravnik, *Phys. Rev. X* **9**, 031051 (2019).
- [50] P. Chandrakar, M. Varghese, S. A. Aghvami, A. Baskaran, Z. Dogic, and G. Duclos, *Phys. Rev. Lett.* **125**, 257801 (2020).
- [51] S. Chandragiri, A. Doostmohammadi, J. M. Yeomans, and S. P. Thampi, *Phys. Rev. Lett.* **125**, 148002 (2020).
- [52] J. Binysh, Ž. Kos, S. Čopar, M. Ravnik, and G. P. Alexander, *Phys. Rev. Lett.* **124**, 088001 (2020).
- [53] L. J. Ruske and J. M. Yeomans, *Phys. Rev. X* **11**, 021001 (2021).
- [54] M. Varghese, A. Baskaran, M. F. Hagan, and A. Baskaran, *Phys. Rev. Lett.* **125**, 268003 (2020).
- [55] A. J. H. Houston and G. P. Alexander, *Phys. Rev. E* **105**, L062601 (2022).
- [56] P. W. Ellis, D. J. Pearce, Y.-W. Chang, G. Goldsztein, L. Giomi, and A. Fernandez-Nieves, *Nat. Phys.* **14**, 85 (2018).
- [57] D. J. G. Pearce, P. W. Ellis, A. Fernandez-Nieves, and L. Giomi, *Phys. Rev. Lett.* **122**, 168002 (2019).
- [58] Y. Maroudas-Sacks, L. Garion, L. Shani-Zerbib, A. Livshits, E. Braun, and K. Keren, *Nat. Phys.* **17**, 251 (2021).
- [59] See Supplemental Material at <http://link.aps.org/supplemental/10.1103/PhysRevE.106.L012602> for movies and additional information.
- [60] D. Marenduzzo, E. Orlandini, M. E. Cates, and J. M. Yeomans, *Phys. Rev. E* **76**, 031921 (2007).
- [61] S. P. Thampi, R. Golestanian, and J. M. Yeomans, *Philos. Trans. R. Soc. A* **372**, 20130366 (2014).
- [62] D. P. Rivas, T. N. Shendruk, R. R. Henry, D. H. Reich, and R. L. Leheny, *Soft Matter* **16**, 9331 (2020).
- [63] N. Aryasova, Y. Reznikov, and V. Reshetnyak, *Mol. Cryst. Liq. Cryst.* **412**, 351 (2004).
- [64] L. Giomi, M. C. Marchetti, and T. B. Liverpool, *Phys. Rev. Lett.* **101**, 198101 (2008).
- [65] I. Delbende, C. Selçuk, and M. Rossi, *Phys. Rev. Fluids* **6**, 084701 (2021).
- [66] Y. S. Song and H. Brenner, *J. Chem. Phys.* **131**, 224108 (2009).
- [67] R. E. Goldstein, I. Tuval, and J.-W. van de Meent, *Proc. Natl. Acad. Sci. USA* **105**, 3663 (2008).
- [68] J.-W. van de Meent, I. Tuval, and R. E. Goldstein, *Phys. Rev. Lett.* **101**, 178102 (2008).
- [69] J. Verchot-Lubicz and R. E. Goldstein, *Protoplasma* **240**, 99 (2010).
- [70] F. G. Woodhouse and R. E. Goldstein, *Proc. Natl. Acad. Sci. USA* **110**, 14132 (2013).
- [71] D. J. G. Pearce, *New J. Phys.* **22**, 063051 (2020).
- [72] G. Napoli and S. Turzi, *Phys. Rev. E* **101**, 022701 (2020).
- [73] S. Hozumi, R. Maeda, K. Taniguchi, M. Kanai, S. Shirakabe, T. Sasamura, P. Spéder, S. Noselli, T. Aigaki, R. Murakami, and K. Matsuno, *Nature (London)* **440**, 798 (2006).
- [74] D. Oriola, F. Jüllicher, and J. Brugués, *Proc. Natl. Acad. Sci. USA* **117**, 16154 (2020).
- [75] M. Novak, B. Polak, J. Simunić, Z. Boban, B. Kuzmić, A. W. Thomae, I. M. Tolić, and N. Pavin, *Nat. Commun.* **9**, 3571 (2018).
- [76] L. Tortora and O. D. Lavrentovich, *Proc. Natl. Acad. Sci. USA* **108**, 5163 (2011).
- [77] V. Koning, B. C. van Zuiden, R. D. Kamien, and V. Vitelli, *Soft Matter* **10**, 4192 (2014).
- [78] K. Nayani, R. Chang, J. Fu, P. W. Ellis, A. Fernandez-Nieves, J. O. Park, and M. Srinivasarao, *Nat. Commun.* **6**, 8067 (2015).
- [79] J. Jeong, L. Kang, Z. S. Davidson, P. J. Collings, T. C. Lubensky, and A. G. Yodh, *Proc. Natl. Acad. Sci. USA* **112**, E1837 (2015).
- [80] J. Słomka and J. Dunkel, *Proc. Natl. Acad. Sci. USA* **114**, 2119 (2017).
- [81] H. K. Moffatt, *J. Fluid Mech.* **914**, P1 (2021).